The International Journal of Advanced Manufacturing Technology
https://doi.org/10.1007/s00170-026-17618-4

ORIGINAL ARTICLE

In situ monitoring and control of laser-directed energy deposition with wire – part 2: geometry and hardness modeling and closed-loop control

Mostafa Rahmani Dehaghani[1] · Kevin Oldknow[2] · Morgan Nilsen[3] · Farzaneh Farhang Mehr[4] · Yifan Tang[1] · Nguyen Gia Hien Vu[1] · Ke Wang[1] · G. Gary Wang[1]

Received: 1 October 2025 / Accepted: 27 January 2026

Abstract
Laser-directed energy deposition with wire (L-DED/W) offers high deposition and material utilization rates but often suffers from geometric inaccuracies and anisotropic mechanical properties due to unstable deposition dynamics and complex thermomechanical phenomena. To enable in situ monitoring and closed-loop control of final qualities such as geometry and hardness—which cannot be directly measured during deposition—this study employs the parameter–signature–quality (PSQ) framework. This work presents the first in situ multi-input multi-output (MIMO) closed-loop control of both deposition geometry and hardness in a directed energy deposition process. Building on the experimental foundation established in Part 1 of this study, a real-time MIMO control strategy is developed for the L-DED/W process. A long-short-term-memory (LSTM) network is used to model the nonlinear and dynamic relationships between process parameters (power and speed) and melt pool signatures, while hardness is classified using a combined set of process parameters and melt pool signatures within the PSQ framework. These models are integrated with a fuzzy logic controller to achieve closed-loop MIMO control, demonstrating effective regulation of melt pool geometry while maximizing the likelihood of achieving high hardness under process uncertainties. The results demonstrate the feasibility of in situ regulation of otherwise unmeasurable final qualities and highlight fuzzy logic control as a flexible and computationally efficient approach for multi-objective control in metal additive manufacturing.

Keywords Laser directed energy deposition with wire · In situ monitoring · Long-Short-Term-Memory · Closed-loop control · Multi-objective control · Fuzzy logic control

1 Introduction

In situ monitoring and closed-loop control of final component qualities have attracted attention as effective strategies for improving the reliability and consistency of parts produced by additive manufacturing (AM). This growing interest is primarily due to challenges associated with developing accurate ex-situ models and the inherent temporal fluctuations observed in metal AM process parameters during fabrication [1–3]. For instance, experimental measurements have shown that the actual laser power (LP) delivered during processing can deviate significantly from the machine setpoint, with reported differences on the order of 7–14% [4]. Such fluctuations introduce uncertainties that ex-situ modeling techniques cannot accurately capture or predict. In response to these challenges, recent

✉ Mostafa Rahmani Dehaghani
mostafa_rahmani_dehaghani@sfu.ca

[1] School of Mechatronic Systems Engineering, Simon Fraser University, Surrey, BC, Canada

[2] School of Sustainable Energy Engineering, Simon Fraser University, Surrey, BC, Canada

[3] Division of Industrial Automation, University West, Trollhättan, Västergötland, Sweden

[4] Department of Materials Engineering, University of British Columbia, Vancouver, BC, Canada

Published online: 09 February 2026

advancements in sensing technologies and control systems have facilitated the implementation of in situ monitoring and control approaches, which effectively mitigate modeling inaccuracies and compensate for real-time uncertainties and parameter variations during the AM process [5, 6].

However, a significant challenge arises when certain final qualities of AM components cannot be directly measured in situ, making them difficult to monitor and control during fabrication. To address this challenge, the parameter–signature–quality (PSQ) framework has been proposed. In this framework, measurable process signatures with strong correlations to the final qualities act as connecting intermediaries between process parameters and component qualities (Fig. 1(a)). The relationship linking process parameters to signatures is denoted as F_1, while the relationship between process signatures and final qualities is denoted as F_2. The general structure of the closed-loop control block diagram within the PSQ framework is illustrated in Fig. 1(b). The parameter–signature model (F_1) is developed through system identification methods, serving either as a process simulator for the controller design or as a foundation for direct control on the actual AM process. Meanwhile, the signature–quality model (F_2) translates sensor signals (process signatures) into final component qualities, which in turn inform the control variables of the closed-loop control system. This approach enables indirect measurement and control of otherwise unmeasurable qualities. For instance, the PSQ framework has been successfully utilized to control bead width (quality) by manipulating LP (parameter) and monitoring melt pool width (MPW) as a process signature in the laser directed energy deposition with wire (L-DED/W) process [7].

This manuscript is the second in a two-part series aimed at developing multi-input multi-output (MIMO) in situ monitoring and control strategies for final qualities such as hardness, geometry, and microstructure in directed energy deposition (DED) processes for duplex stainless steel (DSS) components. In Part 1, systematic experiments were conducted to establish a robust dataset for modeling and control, identify key correlations within the PSQ framework, and introduce image-processing techniques for extracting melt pool and microstructural features [8]. Building on these results, the present study aims to demonstrate the application of the PSQ framework for multi-objective, closed-loop MIMO control of final qualities that are otherwise unmeasurable in situ.

Achieving this objective is realized through three key stages: (i) MIMO system identification to model the parameter–signature relationship (F_1), (ii) modeling the signature–quality relationship (F_2) to enable indirect control of final properties, and (iii) integration of F_1 and F_2 into a closed-loop control architecture. Each stage addresses specific limitations in existing approaches and is discussed in the following.

The first stage involves constructing the F_1 model describing the relationship between process parameters and process signatures. Previous system identification efforts in DED have largely focused on single-input single-output (SISO) formulations, most commonly modeling MPW as a function of laser power using linear transfer functions [9]. Similar linear SISO approaches have been applied in electron beam DED, where the electron beam current is used as the control variable [10]. While these methods provide valuable insights for simplified scenarios, they rely on linear dynamics and neglect the inherently multivariable nature of DED processes, where melt pool behavior is simultaneously influenced by travel speed, deposition rate, material properties, and evolving thermal conditions [11]. To address multivariable interactions, Rahmani Dehaghani et al. [12] introduced a transfer-learning-based MIMO framework that adapts linear source-domain models to target domains under severe data scarcity. However, despite these advances, most MIMO system identification studies in AM continue to rely on linear models, and nonlinear MIMO modeling remains

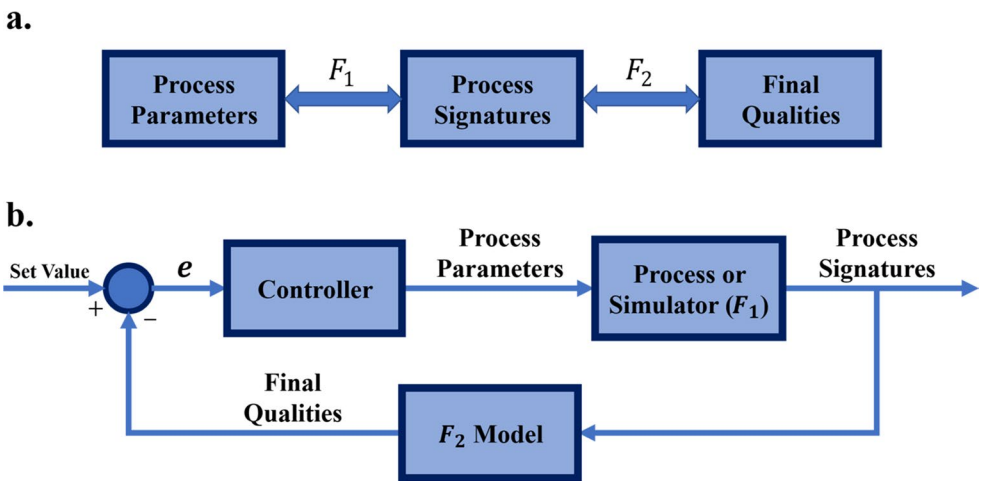

Fig. 1 PSQ framework: (**a**) Process signatures serving as intermediaries between process parameters and final qualities; (**b**) Closed-loop control block diagram

relatively unexplored. In this study, a nonlinear MIMO system identification model is developed using a long short-term memory (LSTM) network to capture the dynamic relationships between laser power, travel speed, and multiple melt pool signatures, including MPW, melt pool length, and melt pool size. Bead number and layer number are incorporated to account for accumulated thermal effects and surrounding geometry, and calibrated input uncertainties are included to better reflect real-world process variability. This model constitutes the F_1 component of the PSQ framework.

The second step focuses on developing the F_2 link of the PSQ framework. Hardness and final bead geometry are set as the primary control objectives. Traditionally, hardness modeling in DED processes has been performed as a function of process parameters [13, 14] which limits its applicability within the PSQ framework. In this study, MPW is used to approximate bead geometry, and hardness modeling is approached as a classification task based on the process parameters and signatures. To further improve predictive accuracy and capture the effect of accumulated thermal history, bead and layer numbers are also incorporated into the model, as they significantly influence microstructural evolution and hardness through repeated heating and cooling. Hardness is categorized into three classes—"High," "Medium," and "Low"—and the 288 data points collected in the first part [8],, are used to develop various classification models, including K-nearest neighborhood (KNN), support vector machine (SVM), artificial neural network (ANN), and ensemble methods.

The final stage integrates the F_1 and F_2 models into a closed-loop control architecture. Closed-loop control of final part qualities, such as microstructure and mechanical properties, has been explored in a limited number of studies. Nassar et al. [15] developed an intralayer control strategy that dynamically modified the build plan to maintain temperature thresholds, resulting in improved microstructural and hardness uniformity. Farshidianfar et al. [16] proposed a closed-loop PID-based approach for laser DEDs with powder, regulating cooling rate through travel speed control to refine microstructure, and later extended this methodology to multilayer walls, achieving improved uniformity despite residual variations [17]. While these studies demonstrate the potential of closed-loop control, they do not explicitly establish a signature–quality relationship, and therefore lack the F_2 link required within the PSQ framework. Fuzzy logic controllers (FLCs) have been shown to be effective in handling nonlinearities and uncertainties in AM processes [18–24], yet their application has largely been limited to controlling geometric features or thermal proxies. In this study, an FLC is integrated with the PSQ framework to enable simultaneous MIMO control of geometry and hardness. The controller leverages the constructed F_1 and F_2 models to regulate melt pool behavior, indirectly maximize hardness, and maintain geometric stability under calibrated input uncertainties.

This study makes several original contributions to the field of in situ monitoring, modeling, and control of DED processes. First, it presents the first demonstration of in situ closed-loop control of hardness in a DED process, achieved indirectly through the PSQ framework. Second, a true MIMO control strategy is developed to simultaneously regulate deposition geometry and mechanical properties, moving beyond the single-objective or single-input approaches commonly reported in the literature. Third, the integration of LSTM networks for nonlinear MIMO system identification and an FLC within the PSQ framework establishes a practical and computationally efficient pathway toward real-time, multi-objective control of additive manufacturing processes.

The remainder of this paper is structured as follows: Section 2 details the methodology for constructing F_1 and F_2, integrating them into the control block diagram, and implementing closed-loop control. Section 3 presents the modeling and control results along with key findings. Finally, conclusions are drawn in Section 4.

2 Methods and materials

The objective of this study is to develop a closed-loop control system for the MIMO L-DED/W process with the dual goals of maintaining MPW, leading to reduced surface waviness and improved geometric accuracy, while maximizing hardness. The dataset used in this study is obtained from the experimental work reported in the first part of this study [8], where an eight-layer, six-bead DSS 2209 ring (230 mm) is fabricated using the L-DED/W process by systematically varying laser power (3550–4150 W) and travel speed (7–13 mm/s). The ring is deposited using 1.2 mm wire at a feed speed of 2 m/min. During deposition, melt pool images are coaxially captured and processed to extract MPW, MPL, and MPS, defined as the melt pool surface observed from a top coaxial view. Post-process hardness measurements are then performed. In this paper, the collected data are first preprocessed and structured for analysis. Subsequently, the F_1 and F_2 models are developed and incorporated into the control scheme to regulate MPW and hardness during ring deposition in the L-DED/W process.

2.1 Data preprocessing for F_1 and F_2 construction

For F_1 development, the extracted melt pool features, MPW, MPL, and MPS are synchronized with travel speed (TS), laser power (LP), bead number (BN), and layer number

(LN) during deposition. Instances where sensors are defective are removed, along with data from no-printing periods and their immediate surroundings, to ensure a continuous dataset at 30 Hz. The output data is then smoothed using a second-order low-pass Butterworth filter with a normalized cut-off frequency of 0.2 times the Nyquist frequency (2/fps). Additionally, a sliding moving average filter with a window size of 10 is applied, averaging each data point with its 10 surrounding values. Finally, both input and output variables are normalized between zero and one to scale the dataset appropriately for F_1 construction.

For F_2, the hardness values from 288 measurement locations are synchronized with the seven process and melt pool features (BN, LN, LP, TS, MPW, MPL, and MPS), forming a dataset suitable for hardness classification.

2.2 MIMO process signature prediction (F_1 construction)

This section aims to establish the parameter-signature relationship between TS, LP, LN, and BN with MPW, MPL, and MPS. To achieve this, various linear and nonlinear time-series models are explored, including linear transfer functions, nonlinear autoregressive models with exogenous input (ARX), nonlinear Hammerstein-Wiener models, and LSTM networks.

Linear transfer functions predict a system's output response by defining relationships between input and output through poles and zeros in the Laplace or Z-domain, making them useful for modeling linear dynamic systems. Nonlinear ARX models incorporate regressors from present and past input values, as well as past outputs, to estimate the current output using techniques such as ANN or polynomial functions. Hammerstein-Wiener models further enhance system modeling by introducing nonlinear input and output blocks around a central linear dynamic system, allowing for the representation of complex nonlinear behaviors while maintaining a structured framework for system identification and control. These models are trained on 80% of the dataset, with the remaining 20% reserved for testing, and their accuracy is evaluated using the R-squared value to assess their effectiveness in MIMO system identification for the L-DED/W process.

RNN-LSTM models are advanced neural networks designed to capture temporal dependencies in sequential data. RNN models process inputs sequentially, maintaining an internal state that allows them to model time-dependent relationships. However, standard RNNs suffer from vanishing gradient issues, limiting their ability to learn long-term dependencies. LSTM networks address this limitation by incorporating memory cells with gating mechanisms that regulate information flow, enabling the capture of both short- and long-term dependencies. These properties make LSTM models highly effective for system identification and predictive modeling in dynamic processes like DED. The LSTM model is trained using a 70/15/15 split for training, validation, and testing, respectively. The validation set is used for early stopping— with a tolerance of 1e-5 and a patience value selected during fine-tuning—to prevent overfitting and to optimize the model architecture and hyperparameters. Each LSTM layer is complemented by a dropout layer with a ratio of 0.4, enhancing generalization and preventing overfitting. Training is conducted over 100 epochs, and the R-squared serves as the evaluation metric. Among all the models developed, the one demonstrating the highest accuracy is chosen as the F_1, modeling the link between process parameters and melt pool signatures. Its final accuracy is evaluated on the test dataset.

2.2.1 Process parameter uncertainty calibration

As the selected time-series model serves as a simulator for the L-DED/W process, it is essential to incorporate process uncertainties, given that DED inherently involves variations in input parameters. To achieve a more realistic simulation, Gaussian white noise is introduced into TS and LP, mimicking process fluctuations. The uncertainty calibration process involves defining the Uncertainty Calibration Variables (UCVs) as:

$$UCVs = (\sigma_{TS},\ \sigma_{LP}) \tag{1}$$

where, σ_{TS} and σ_{LP} represent the standard deviations of the Gaussian noise added to TS and LP, respectively. Upon application of the UCVs to the model, the output is derived using Monte Carlo Simulation (MCS). This involves averaging 100 predictions for any given input. Additionally, the uncertainty in the model's output is quantified by calculating the standard deviation of these 100 output responses. The UCVs are calibrated using the validation dataset by solving an optimization problem designed to minimize the Mean Squared Error (MSE) between the experimental data and the calibrated model outputs determined by MCS:

$$UCVs^* = \min_{UCVs} \frac{\sum_{i=1}^{n}(y_{exp}^2 - y_{MCS}^2)}{n} \tag{2}$$

subject to:

$$0 \leq \sigma_{LP} \leq 180\,W,\ 0 \leq \sigma_{TS} \leq 1.8\frac{mm}{s}$$

where, y_{exp} and y_{MCS} represent the experimental and calibrated model outputs determined by MCS, respectively, and

n is the number of validation data points. The upper bounds for the UCVs are set to 30% of the range of each parameter, but will be adjusted if they are found to be active after. The optimized uncertainty values, $UCVs^*$, define the noise levels that best replicate real process variations.

This optimization problem is solved using Bayesian optimization, with 10 randomly initialized points and a maximum of 100 function calls. Once calibrated, the uncertainty-calibrated model serves as the simulator of cylindrical feature deposition in the L-DED/W process, forming the foundation for controller design in subsequent sections.

2.3 Hardness classifier development (F_2 construction)

The next step is to establish the signature-quality link in the PSQ framework. Hardness values are classified into three categories: "Low," "Medium," and "High," each covering one-third of the measured hardness range. The corresponding ranges are 244–268 HB for "Low" hardness, 269–292 HB for "Medium" hardness, and 292–316 HB for "High" hardness. The dataset consists of 288 data points, with 10% (28 points) reserved for testing and the remaining 90% used for training with 5-fold cross-validation. Seven features—BN, LN, TS, LP, MPW, MPL, and MPS—are available for classification. However, some features may not contribute significantly to model accuracy. Therefore, feature selection is performed to identify the subset yielding the highest classification performance.

Four modeling approaches—SVM, ANN classifiers, KNN, and ensemble models with decision tree learners—are explored to classify hardness based on process parameters and melt pool signatures. Table 1 summarizes the hyperparameters for each model, distinguishing between fixed and optimizable parameters. The latter are fine-tuned using hyperparameter optimization (HPO), with defined search ranges and possible values listed in Table 1. HPO aims to identify the optimal set of hyperparameters that maximize classification accuracy on the 5-fold cross-validation data. Bayesian optimization is employed for this purpose, selecting hyperparameters in each iteration based on a probabilistic model that balances exploration (searching uncertain regions) and exploitation (focusing on high-performing areas). After selecting a set of parameters, the optimizer trains the model and evaluates its classification accuracy, and proceeds to the next iteration. To determine the appropriate number of iterations, values ranging from 20 to 300 are tested. The results indicate that 100 iterations provide convergence across all models, ensuring an optimal trade-off between computational efficiency and performance.

SVM models classify data by finding the optimal hyperplane for separating classes. Kernel functions—including Gaussian, linear, quadratic, and cubic—handle nonlinearity, while the box constraint (C) controls the trade-off between maximizing margin and minimizing classification errors. Multiclass classification is managed through either a one-vs-one or one-vs-all approach. ANN classifiers process data through interconnected layers of neurons, with architectures limited to three hidden layers to balance computational efficiency and model complexity. KNN classification is based on the majority class of the k nearest neighbors, with k optimized during training. The Euclidean distance metric is fixed for proximity measurements. Ensemble models with decision tree learners combine multiple decision trees to improve classification performance. AdaBoost is used as the ensemble method, adjusting tree weights iteratively for higher accuracy. The maximum number of splits defines tree depth, while the number of learners determines the ensemble size.

The final model is selected based on the highest classification accuracy from various model-feature combinations. Its performance is then evaluated on the test data. Once

Table 1 Hyperparameters of the classification models, including fixed values and optimizable parameters with their respective search ranges

Model	Hyperparameter	Optimizable	Parameter value or range
Support vector machine	Kernel function	Yes	Gaussian, linear, quadratic, cubic
	Box constraint (C)	Yes	[0.001, 100]
	Multiclass coding	Yes	One-vs-one, one-vs-all
ANN Classifier	Number of layers	Yes	1, 2, or 3
	Layer sizes (first, second, third)	Yes	Integers in range [1, 300]
	Activation function	Yes	ReLU, Tanh, Sigmoid, Identity
	Regularization (Lambda)	No	0
K-nearest neighborhood	Number of neighbors (k)	Yes	Integer in range [1, 20]
	Distance metric	No	Euclidean
	Distance weight	Yes	Equal, inverse, or squared inverse
Ensemble decision tree	Ensemble method	No	AdaBoost
	Learner type	No	Decision tree
	Maximum number of splits	Yes	Integer in range [1, 130]
	Number of learners	Yes	Integer in range [10, 500]
	Boosting learning rate	Yes	[0.001, 1]

the best model is selected, partial dependence plots, which represent the marginal effect of individual input features on the predicted classification scores while keeping other variables constant, are generated to visualize how classification scores vary with different process parameters and melt pool signatures. These insights serve two purposes: validating whether the final model aligns with experimental findings and uncovering additional relationships crucial for the controller design.

2.4 Closed-loop control of L-DED/W process using PSQ framework

The control algorithm utilized in this section is primarily an FLC, which is a type of fuzzy inference system (FIS) illustrated in Fig. 2. A FIS operates by first converting crisp inputs into fuzzy sets through fuzzification, using predefined membership functions (MFs) to represent input variables (e.g., "low," "medium," or "high") and handle uncertainty. These fuzzy inputs are then evaluated using a set of "if-then" fuzzy logic rules, which define the interactions between inputs to generate fuzzy outputs (e.g., *if the temperature is high and the speed is medium*, *then the power is low*). Finally, the fuzzy outputs are transformed back into crisp values through defuzzification, yielding actionable outputs for practical applications. This approach facilitates intuitive decision-making in systems where precise mathematical models are either impractical or subject to uncertainty.

What distinguishes an FLC from other FIS implementations is its specific design for controlling system outputs, whether a final quality such as hardness, the output error relative to a setpoint (E), or the change in error (ΔE). The FLC output serves as the input to the plant; however, to enhance control stability, it is often more effective for the FLC to output the change in the input value rather than the absolute input itself. In this case, an integrator with a tunable gain is added after the controller to optimize performance.

The objective of this section is to implement MIMO closed-loop control of MPW and hardness in the L-DED/W process. As an initial step, the FLC is first designed and tested in a simplified SISO control scenario, where LP is the manipulated variable and MPW is the controlled output. Once validated, the control strategy is expanded to a full MIMO framework, where both TS and LP serve as manipulated variables, while MPW and hardness are the controlled outputs. The integration of F_1 and F_2, controller design, and simulations to test various scenarios are all performed in MATLAB and Simulink. Each stage of this development is detailed in the following subsections.

2.4.1 SISO closed-loop control of MPW using FLC

This initial step aims to understand the design and functionality of the FLC in regulating the desired system output, MPW. Maintaining a consistent MPW ensures a uniform final geometry in the printed part, making geometry control the primary objective of this section within a SISO system. The inputs to the FLC are the MPW error relative to the setpoint, defined as $E_{MPW} = MPW - MPW_{set}$, and the change in error, $\Delta E_{MPW} = E_{MPW,t} - E_{MPW,t-1}$. Each input can take different values, so three MFs are defined: negative (N), zero (Z), and positive (P).

In the L-DED/W process, MPW closely approximates the laser spot diameter. Given that a 5 mm laser spot diameter was used in the experiments, MPW in the simulation is around 5 mm, with variations of up to ±1 mm. Consequently, the range for E_{MPW} and ΔE_{MPW} is set to [−1, 1]. The selected MF type for the input variables is triangular. The controller output is the change in LP, ΔLP. To achieve better process control, five MFs are defined for ΔLP: negative big (NB), negative medium (NM), zero (Z), positive medium (PM), and positive big (PB). The range for ΔLP is set to [−600, 600] W to allow the controller to increase or decrease the LP across the full range set for the simulator which is 600 W. The output MFs are also triangular.

With two inputs, each having three MFs, the system comprises nine possible configurations ($3 \times 3 = 9$), leading to nine fuzzy rules defining the controller's response. Since MPW and LP share a monotonic relationship, FLC can effectively regulate MPW with a simple rule set in a closed-loop control scheme. The rules are presented in Table 2, where Table 2(a) represents them in a tabular format, while Table 2(b) presents the matrix format, which is preferred when dealing with more than two inputs, as in the next

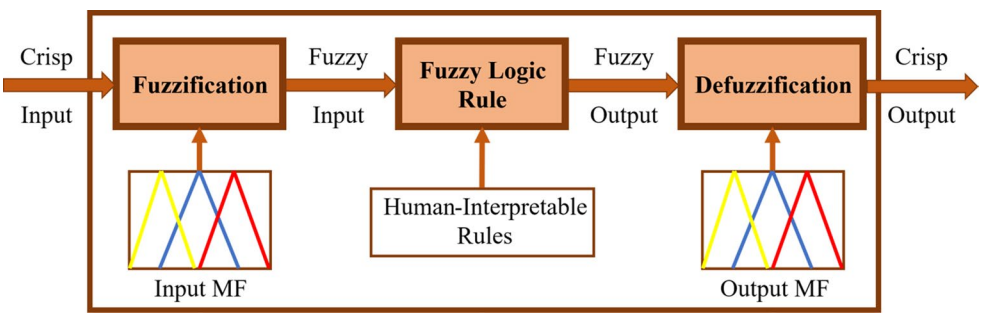

Fig. 2 Fuzzy inference system (FIS) structure

Table 2 The rule set applied to the FLC. (a) table representation. (b) matrix representation

a.		ΔE_{MPW}			b.	Rule No.	E	ΔE	ΔLP
		N	Z	*P*		Rule 1	1	1	1
E_{MPW}	**N**	NB	NM	Z		**Rule 2**	2	1	2
	Z	NM	Z	PM		**Rule 3**	3	1	3
	P	Z	PM	PB		**Rule 4**	1	2	2
						Rule 5	2	2	3
						Rule 6	3	2	4
						Rule 7	1	3	3
						Rule 8	2	3	4
						Rule 9	3	3	5

section. In the matrix format, each MF level is numerically indexed (e.g., 1 corresponds to the first MF, 2 to the second).

The rules are constructed to maintain both E_{MPW} and ΔE_{MPW} at zero. Big output MFs are triggered when both inputs indicate the same control direction. For instance, if both E_{MPW} and ΔE_{MPW} are negative (N), the controller output (ΔLP) should significantly decrease, thus the negative big (NB) MF is selected. Conversely, the zero (Z) output MF is used when both inputs are zero or when their suggested actions conflict (e.g., one calls for an increase, the other for a decrease in ΔLP). When one input is zero, the controller responds based on the non-zero input. It is also important to note that all rules are assigned equal weight.

The FLC utilizes a Mamdani-type fuzzy inference system with centroid defuzzification. Figure 3(a) summarizes the FLC designed for SISO closed-loop control of MPW.

The performance of the FLC is evaluated against a proportional-integral (PI) controller, which is designed under the same conditions. The proportional and integral gains of the PI controller are tuned using a grid search, each ranging from 1 to 100,000. Figure 3(b) illustrates the closed-loop control block diagram used for this comparison. The simulation sampling time is set to 1/30 seconds, matching the data acquisition frequency in the experiments. Additionally, K_{LP} in the integrator serves as a gain to scale the controller output, with its optimal value determined through a grid search within the range of 0.5 to 1000.

The comparison is conducted by simulating the deposition of a two-layer single-bead ring with a diameter of 100 mm, maintaining a constant travel speed of 10 mm/s. The evaluation focuses on overshoot percentage, steady-state error, and rise time, providing a direct performance comparison between the PI controller and the FLC. The comparison results are presented in Section 3.

2.4.2 MIMO closed-loop control of MPW and hardness using PSQ and FLC

The FLC developed in the previous section is expanded to a MIMO L-DED/W system to simultaneously control MPW and maximize hardness. The manipulated variables are LP and TS. The inputs to the FLC include E_{MPW} and ΔE_{MPW}, as previously defined, along with an additional input parameter: high-class residual confidence (R_{HC}), defined as:

$$R_{HC} = r_{high} - \max(r_{med},\ r_{low}) \tag{3}$$

where r_{low}, r_{med}, and r_{high} represent the classification scores for the corresponding three hardness categories. R_{HC} quantifies how much the confidence in the "High" hardness classification exceeds that of the next most probable category. A positive R_{HC} indicates that the model predicts "High" hardness, which is the desired outcome. A negative R_{HC} suggests that the model predicts a hardness category other

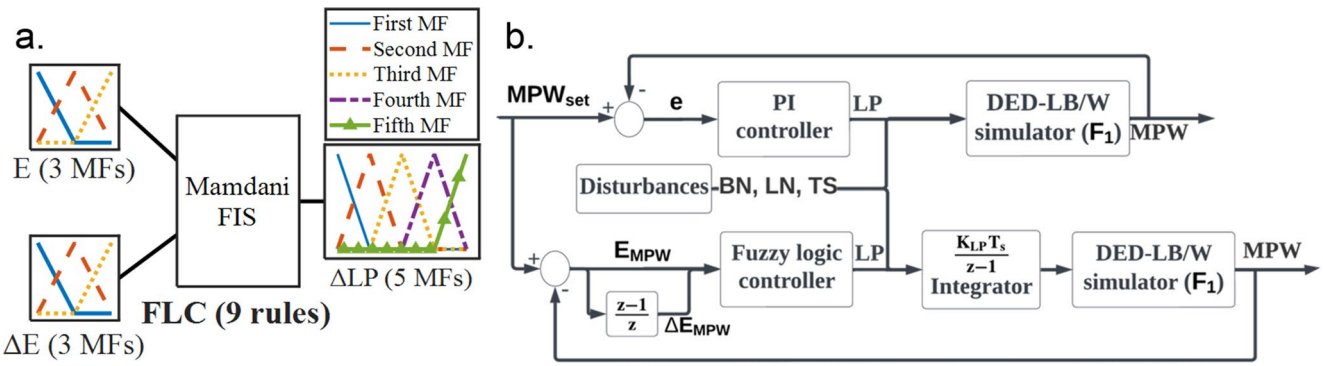

Fig. 3 Comparing two controllers for MPW: (**a**) FLC structure for SISO L-DED/W system control. (**b**) Closed-loop PI control block diagram

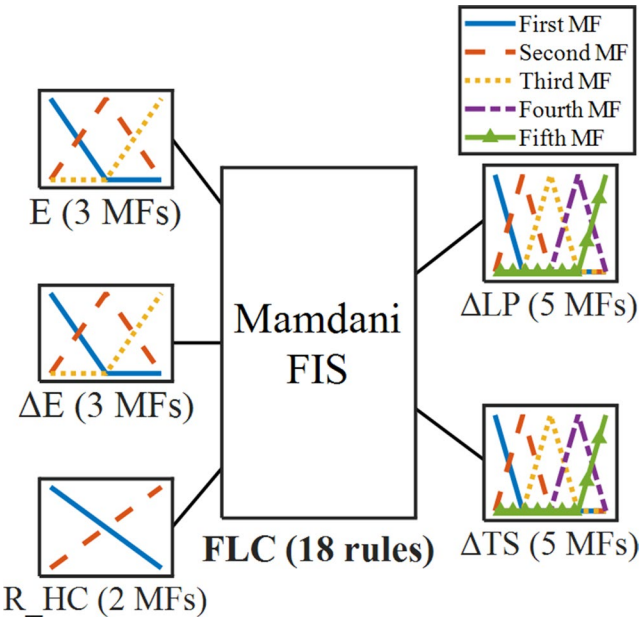

Fig. 4 FLC structure for the MIMO L-DED/W system control

than "High." The primary objective is to maintain a positive R_{HC} and maximize it to increase the likelihood of achieving higher hardness.

To implement this, two MFs are defined for R_{HC}: negative (N) and positive (P). Since maintaining an R_{HC} close to zero is not a desired outcome, a zero-MF is not included. The MFs for R_{HC} are linear ramps with saturation, with a defined range of [−1,1]. The MFs for E_{MPW} and ΔE_{MPW} retain the same shape as before but with variable ranges, $[-r_E, r_E]$ and $[-r_{\Delta E}, r_{\Delta E}]$, respectively. These range limits are not fixed because the robustness and performance of the controller are highly dependent on the appropriate scaling of input MFs. The parameters r_E and $r_{\Delta E}$ are included as optimization variables to enhance controller performance.

For the FLC outputs, five MFs are defined for TS, similar to LP. The MFs for TS are triangular, with a range of [−6, 6] mm/s, corresponding to the experimental TS range. The total number of rules in the expanded FLC is 18, given by the combination of three MFs for E_{MPW}, three for ΔE_{MPW}, and two for R_{HC} ($3 \times 3 \times 2 = 18$). The specific rule set is determined after the F_2 function is developed, allowing for a better understanding of input-output relationships. The structure of the FLC for the MIMO L-DED/W system control is illustrated in Fig. 4.

The next step is to integrate the FLC with the F_1 and F_2 models to regulate MPW and maximize hardness. This integration is depicted in the closed-loop control block diagram in Fig. 5. In this framework, two disturbances, BN and LN, represent variations in the printing location.

The FLC receives three inputs: E_{MPW}, ΔE_{MPW}, and R_{HC}, and generates two outputs: the changes in TS and LP. These outputs are then processed through integrators to compute the updated LP and TS values. The integrators include adjustable gains, K_{LP} and K_{TS}, which are optimization parameters that influence controller performance. To ensure stability and feasibility, upper and lower saturation limits are imposed on the integrators, corresponding to the allowable LP and TS ranges. The L-DED/W simulator, represented by the F_1 model, predicts melt pool characteristics based on the updated process parameters. Meanwhile, the classification model estimates hardness scores for each category, from which R_{HC} is computed and fed back to the controller alongside E_{MPW} and ΔE_{MPW}, closing the control loop.

The FLC is fine-tuned using a self-developed code and a genetic algorithm (GA) to minimize the sum of absolute E_{MPW} over a 10-second simulation period, while fixing BN and LN values at one for simplicity. MPW_{set} follows a square waveform with a bias of 5.05 mm, an amplitude of 0.15 mm, and a frequency of $2\pi/5$ rad/sec to introduce controlled variations. The objective is to optimize r_E, $r_{\Delta E}$, K_{TS}, and K_{LP}, along with specific rule adjustments (detailed in the results section), to achieve the lowest possible sum of absolute E_{MPW}. Finally, the input uncertainties identified

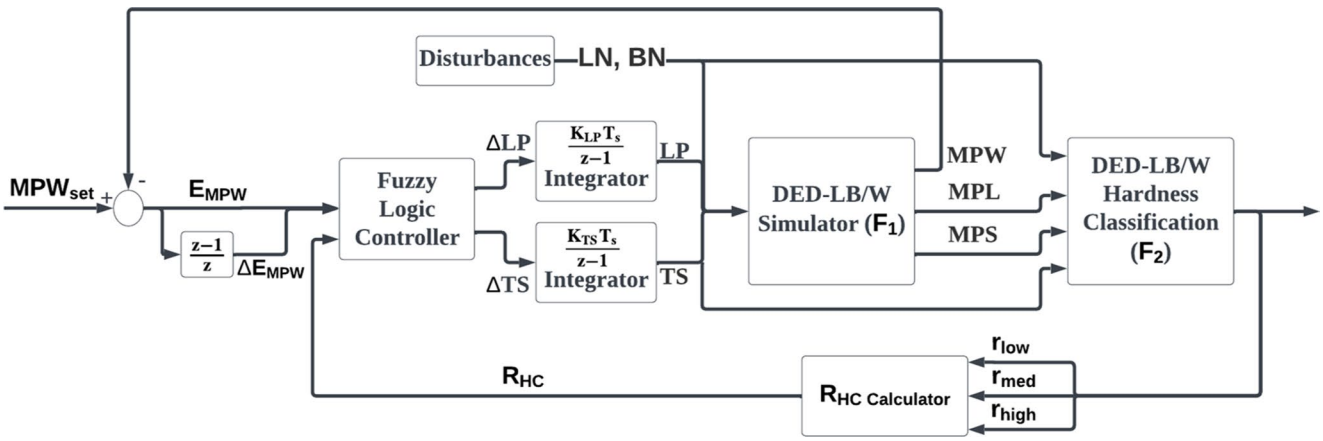

Fig. 5 Closed-loop control block diagram of MIMO L-DED/W for hardness and MPW control using the PSQ scheme

during system identification (σ_{LP}, σ_{TS}) are incorporated into the simulation to better approximate real-world conditions.

3 Results and discussion

3.1 MIMO process signature prediction (F_1 construction)

Printing the DSS 2209 ring with eight layers and six beads, while systematically varying process parameters and capturing coaxial melt pool images as detailed in [8], yields 105,080 images at a 30 fps frequency. From these, MPW, MPL, and MPS data are extracted. Preprocessing and data cleaning reduce the data points to 93,612. MPW, MPL, and MPS data are normalized and synchronized with BN, LN, TS, and LP, ready for modeling.

Various configurations of linear transfer functions (with up to three poles), ARX, and Hammerstein-Wiener models are constructed on the training data. However, their R-squared values do not exceed 0.432 for any of the outputs, highlighting the complexity and nonlinearity inherent in the dataset and associated with the intricacies of the L-DED/W process. Although some studies indicate that the relationship between MPW and LP can be effectively modeled by linear approaches [7, 9], these models fall short with the new dataset. This dataset, reflecting more complex behaviors due to increased material deposition and rapid modifications in process parameters—including factors like heat accumulation—affects melt pool morphology and dynamics. In conclusion, these employed models are not sufficiently flexible to capture the full range of complexities involved in high-volume builds, thus rendering them ineffective for predicting melt pool morphology.

The LSTM model is then employed to model the dynamic relationship between process parameters and their corresponding signatures. Before modeling begins, sequences of input data are prepared. The LSTM utilizes past input parameters to forecast future system outputs, with the 'time steps' indicating the number of past data points considered for predictions. This hyperparameter, critical to model performance, dictates how far back the network looks to learn and predict future outcomes. Time steps require careful tuning to optimize model accuracy. Table 3 presents a summary of the LSTM architecture, hyperparameter fine-tuning, and the R-squared values obtained on validation data for various outputs. In addition, more than 40 other combinations of hyperparameters—including different selections of time steps ranging from 10 to 200—were tested but are not included in the table, as they would make the table excessively long.

According to Table 3, the model with training number 11 outperforms others, demonstrating superior R-squared values of 0.800, 0.909, and 0.821 for MPW, MPL, and MPS respectively on validation data. This commendable accuracy establishes the model as the F_1 link within the PSQ framework, and it is subsequently used in further sections. Figure 6 illustrates the training and validation loss of this model, highlighting that training is halted at epoch 25 as continued training does not yield substantial improvements in validation accuracy.

The model is employed for uncertainty calibration of the process parameters to identify $UCVs^*$ using Eq. 2. A pertinent question arises: does including uncertainty deteriorate model accuracy? This query is addressed by examining Fig. 7, where the horizontal red dashed line indicates the R-squared value of the model without any uncertainty calibration, and the blue solid line represents the R-squared values on the validation MPS data when different standard deviations are applied for MCS. The x-axis of the figure denotes the standard deviation applied to the normalized data, with 0.1 indicating that the applied UCVs are (0.1, 0.1). It becomes apparent that applying uncertainty calibration not only makes the model more reflective of actual

Table 3 LSTM model architecture and hyperparameter fine-tuning evaluated on the validation data

No.	Early stopping, patience	Neurons	LSTM layers	Time steps	*R*-squared		
					MPW	MPL	MPS
1	Yes, 10	50	4	80	0.660	0.738	0.813
2	No	50	4	80	0.532	0.512	0.728
3	Yes, 20	50	2	80	0.545	0.501	0.781
4	Yes, 20	50	1	80	0.532	0.667	0.741
5	Yes, 20	50	1	80	0.654	0.672	0.793
6	Yes, 30	100	1	80	0.632	0.663	0.743
7	No	150	1	80	0.305	0.620	0.772
8	Yes, 25	100	1	40	0.716	0.735	0.796
9	Yes, 35	75	1	60	0.758	0.801	0.812
10	Yes, 35	100	1	80	0.676	0.869	0.772
11	**Yes, 35**	**75**	**1**	**80**	**0.800**	**0.909**	**0.821**
12	Yes, 35	75	1	120	0.698	0.812	0.749

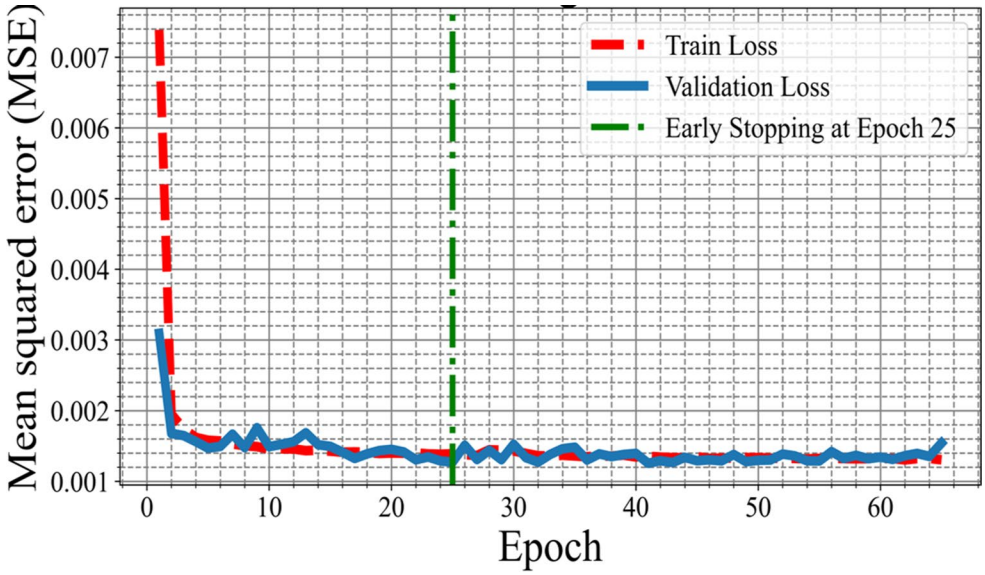

Fig. 6 Training and validation loss trends for the LSTM model during training

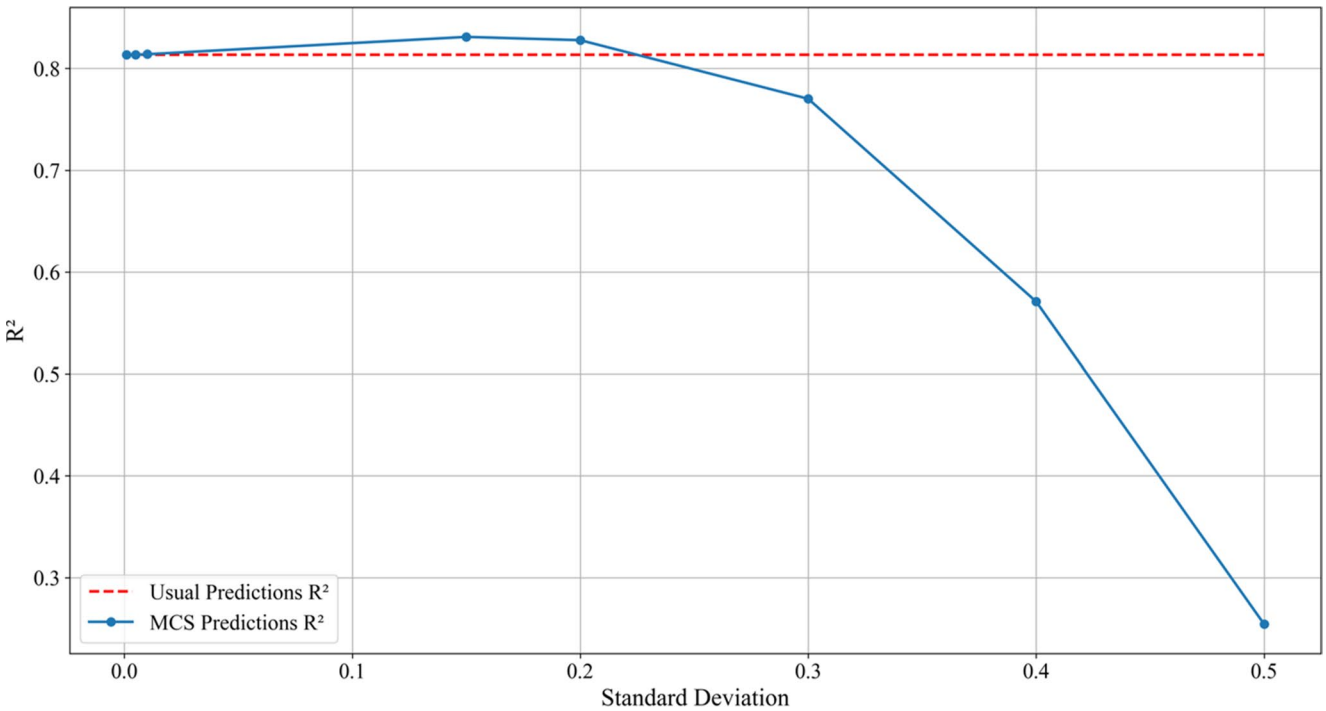

Fig. 7 Comparison of model accuracies without uncertainty calibration and with uncertainty-calibrated models on MPS validation data

conditions but also enhances the model's accuracy, as evidenced by the blue solid line surpassing the red dashed lines at certain standard deviations. This trend is similarly observed in the other two outputs, MPW and MPL.

After performing the uncertainty calibration, the optimized parameters are identified as follows:

$$UCVs^* = (0.3726\frac{mm}{s},\ 114.96\,W) \tag{4}$$

These calibrated uncertainties are then utilized in process simulations, allowing for a more realistic representation of variations in the L-DED/W process. The model's outputs, both with and without the applied uncertainty, are compared against the test data for all three outputs in Fig. 8. The gray uncertainty range in these figures represents the standard deviation of the 100 output responses obtained through MCS. Figure 8 highlights two key findings. First, it demonstrates the effectiveness of LSTM models in capturing

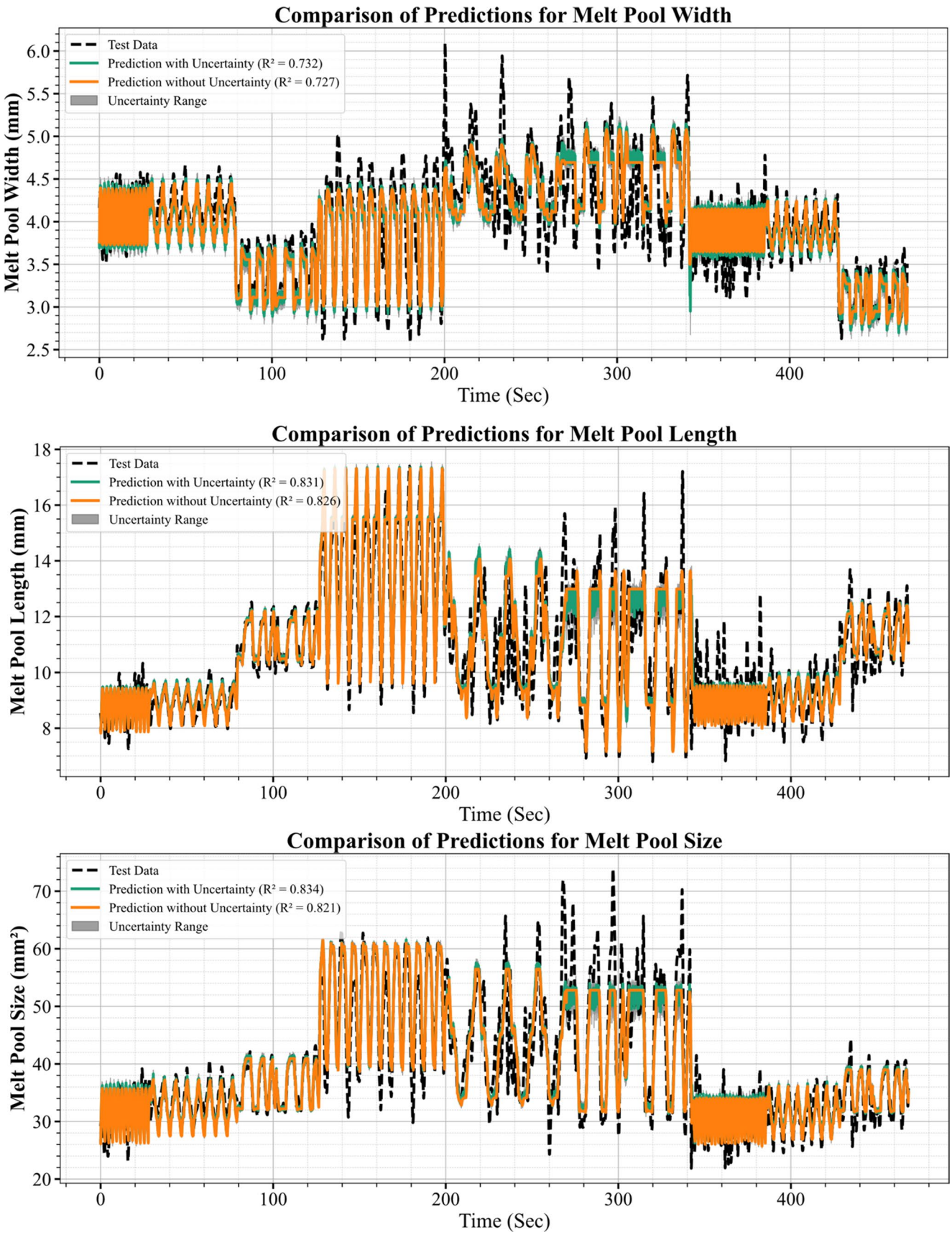

Fig. 8 Evaluation of LSTM model performance on melt pool features prediction with and without uncertainty calibration using test data

temporal dependencies within the L-DED/W process. The model achieves R-squared values of 0.727, 0.826, and 0.821 for MPW, MPL, and MPS, respectively, on the test data without uncertainty calibration—showcasing strong predictive performance. This is further supported by the close alignment between the test data and the LSTM model's "Prediction without Uncertainty," which follow similar trends. The second key takeaway from Fig. 8 is the successful implementation of uncertainty calibration. Not only did the R-squared values remain stable, but they slightly improved, reaching 0.732, 0.831, and 0.834 for MPW, MPL, and MPS, respectively. This enhancement suggests that incorporating uncertainty into the model improves robustness without compromising accuracy. Such robustness is crucial when designing a controller for the L-DED/W process, ensuring that the model remains reliable under real-world process variations.

3.2 Hardness classification model development (F_2 construction)

The construction of hardness classification models follows the procedure outlined in Table 1. Table 4 provides a summary of the selected features, hyperparameter values, and accuracies of notable models evaluated using 5-fold cross-validation. Hyperparameters are optimized through HPO, while features are manually selected to evaluate different configurations.

Particularly for the ANN classifier models, it becomes clear that the model incorporating the five features—LN, BN, TS, MPL, and MPS—achieves the highest accuracy (Accuracy = 74.6%). This finding is consistent across different model types; for instance, the ensemble model utilizing these five features outperforms other ensemble models. This outcome confirms that LN, BN, TS, MPL, and MPS are the optimal features for classifying hardness with the highest

Table 4 Accuracies of developed hardness classifier models using 5-fold cross-validation

Model	Features	Hyperparameters	Accuracy (%)
ANN Classifier	LN, BN, TS, LP, MPW, MPL, MPS	Layers and neurons: [3]* Activation: ReLU	51.5
	LN, BN, TS, MPL, MPS	**Layers and neurons: [18]** **Activation: Sigmoid**	**74.6**
	LN, TS, MPL	Layers and neurons: [5, 19] Activation: Sigmoid	61.9
	LN, MPL, MPS	Layers and neurons: [6, 21, 5] Activation: ReLU	49.2
SVM	LN, BN, TS, MPL, MPS	Kernel: Cubic, C = 0.76 Multiclass: One-vs-one	68.9
	LN, BN, TS, MPL	Kernel: Gaussian, scale = 1.86, C = 35.37 Multiclass: One-vs-all	58.8
Ensemble trees	LN, BN, TS, MPL, MPS	Ensemble method: Bag Max. number of splits: 16 Number of learners: 18	68.3
	LN, BN, TS, MPL, MPW	Ensemble method: Bag Max. number of splits: 24 Number of learners: 15	60.8
	LN, BN, TS, LP, MPL	Ensemble method: Bag Max. number of splits: 14 Number of learners: 10	57.7
	LN, BN, TS, MPL	Ensemble method: Bag Max. number of splits: 174 Number of learners: 10	52.3
KNN	LN, BN, TS, LP, MPL	Number of neighbors: 56 Distance weight: Inverse	59.6
	LN, BN, TS, MPL, MPS	Number of neighbors: 47 Distance weight: Inverse	63.5
	LN, BN, TS, LP, MPW, MPL, MPS	Number of neighbors: 20 Distance weight: Inverse	60.4
	LN, BN, TS, MPL	Number of neighbors: 130 Distance weight: Inverse	56.2

* [18] = one layer with 18 neurons; [15, 19] = two layers with 15 and 19 neurons, respectively

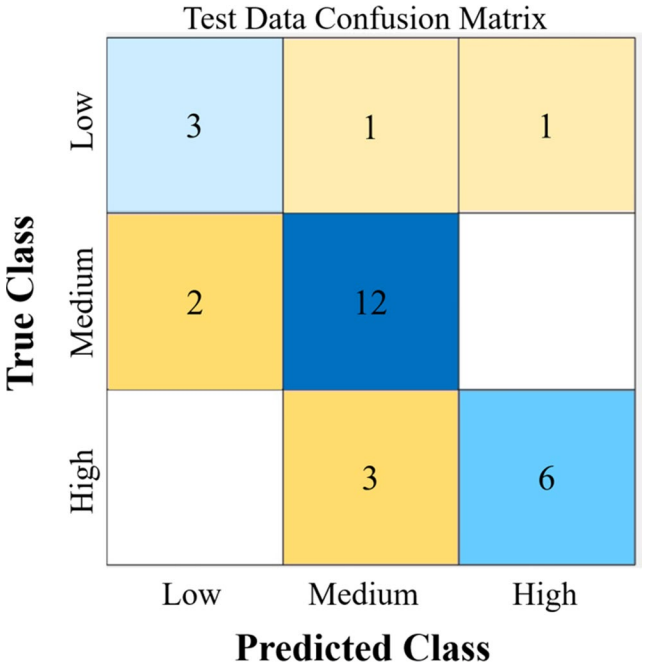

Fig. 9 Confusion matrix of the hardness classification model on the test data

accuracy, aligning with insights from the first part of this study [8], where MPW and LP were found to lack correlation with hardness or microstructure.

The most accurate model is identified as the second ANN classifier, which includes one layer and 18 neurons, also known as the extreme learning machine (ELM) due to its single-layer architecture.

Figure 9 displays the confusion matrix for the selected model evaluated on the test data. The dominance along the diagonal of the confusion matrix indicates the model's robust performance. Additionally, the model's test accuracy, calculated as $\frac{6+12+3}{28} \times 100 = 75\%$, closely aligns with the cross-validation accuracy of 74.6%, suggesting that the model is not overfitted. While no prior study was found specifically targeting hardness classification from process parameters and signatures in additive manufacturing, the achieved accuracy is promising given the complexity of the DED process, the inherent uncertainties in thermal history, and the limited size and balance of the dataset. In particular, the dataset contains fewer samples in the "High" and "Low" hardness categories, making classification more difficult for these minority classes. The current model offers a fast and lightweight alternative to more expensive multiphysics-based simulations, which themselves often require extensive calibration and still face challenges in achieving highly accurate hardness predictions. In this context, a ~ 75% classification accuracy offers meaningful predictive capability for guiding PSQ understanding in DED processes.

To further evaluate the influence of selected features, particularly process parameters and signatures on hardness, and to verify the model's performance, partial dependence plots of the selected model are illustrated for TS and MPL in Fig. 10 for both High and Low hardness classes. It is observed that the likelihood of achieving high hardness increases with an increase in TS, as evidenced by the rising classification scores for the high hardness class. This result is expected and plays a crucial role in controlling hardness. Similarly, a decrease in MPL correlates with an increase in the high-class hardness score, consistent with the findings of the first part of the study [8], where it was shown that increasing TS, which leads to a decrease in MPL, ultimately results in higher hardness. These observations highlight the critical role of MPL as a signature in both modeling and control. Its inclusion not only improves prediction accuracy but also enables meaningful interpretation and real-time

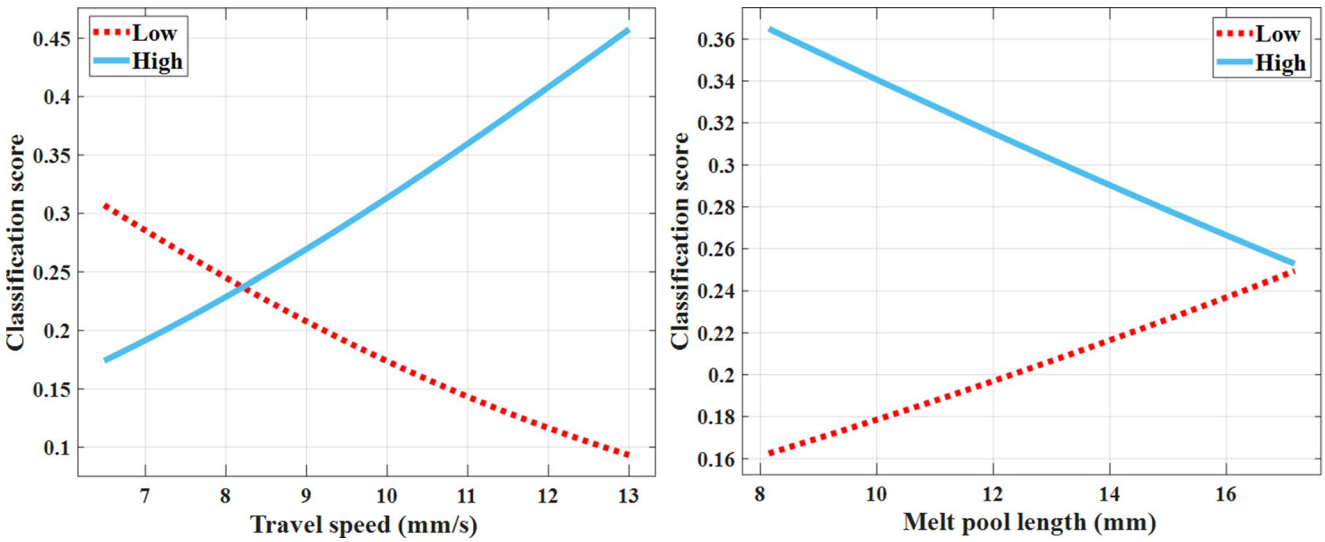

Fig. 10 Partial dependence plots of the classification model for TS (left) and MPL (right) are depicted for "Low" and "High" hardness classes

intervention in the process—thereby reinforcing the effectiveness of using process signatures in closed-loop quality control.

The insights gained from this section are instrumental in applying MIMO closed-loop control. It becomes clear that LP and MPW do not play a direct role in the hardness classification model, as they are excluded from the model, allowing LP to be specifically utilized to control MPW without impacting hardness. Furthermore, to increase the likelihood of achieving high hardness, it is advisable to increase TS as much as possible, provided that this increase does not conflict with other process objectives.

3.3 Closed-loop control of L-DED/W process

The RNN-LSTM model is utilized as the F_1 link and the ELM classifier as the F_2 within the PSQ framework, both integrated into the closed-loop control simulation of the process performed in MATLAB. A zero-order hold with a sampling frequency of 30 Hz is also applied to mimic the data acquisition of a real machine. Both SISO and MIMO control schemes are simulated, with the results presented in the following subsections.

3.3.1 SISO closed-loop control of MPW using FLC

Following the integration of the FLC and PI controllers with the L-DED/W process simulator, as outlined in the closed-loop control block diagram shown in Fig. 3(b), the integrator gains for the FLC (K_{LP}) and the proportional and integral gains for the PI controller (K_P and K_I) are tuned. Optimal gain values are determined through a grid search aimed at minimizing the rise time for both controllers, yielding the following settings:

$$(K_{LP},\ K_P,\ K_I) = (75,\ 2000,\ 50000)$$

Both controllers are then applied to a two-layer, 100 mm-diameter ring printing simulation to regulate the MPW of the SISO L-DED/W process. Fig. 11 illustrates a comparison between the FLC and PI controllers. The initial MPW setting is 5.2 mm, adjusted to 5.4 mm mid-way through the first layer (at 15.7 s) and reverted to 5.2 mm in the middle of the second layer (at 47.1 s). A disturbance noted at 31.4 s corresponds to the transition from the first to the second layer. The controllers' performance across these scenarios is compared in three inset plots in Fig. 11, showing both controllers achieve zero steady-state error and similar rise times, albeit with some overshoot. Notably, the FLC exhibits marginally lower overshoot during the first set point change (20% vs. 23%) and significantly lower in the second setpoint change, as shown in the lower right inset plot (10% vs. 22%). In terms of disturbance rejection (depicted in the upper right inset plot), the FLC demonstrates quicker settling times, albeit with a slightly higher overshoot.

Overall, the FLC outperforms the PI controller due to its lower overshoot and shorter settling times. This comparison underscores the effectiveness of the FLC in controlling the L-DED/W process, leveraging only a basic understanding of the process's positive relationship between LP and MPW. The distinct behaviors of the controllers during the setpoint changes highlight the system's nonlinearity, which poses greater challenges for the PI controller, especially given the extensive tuning required when a linearized model of the plant is not accessible.

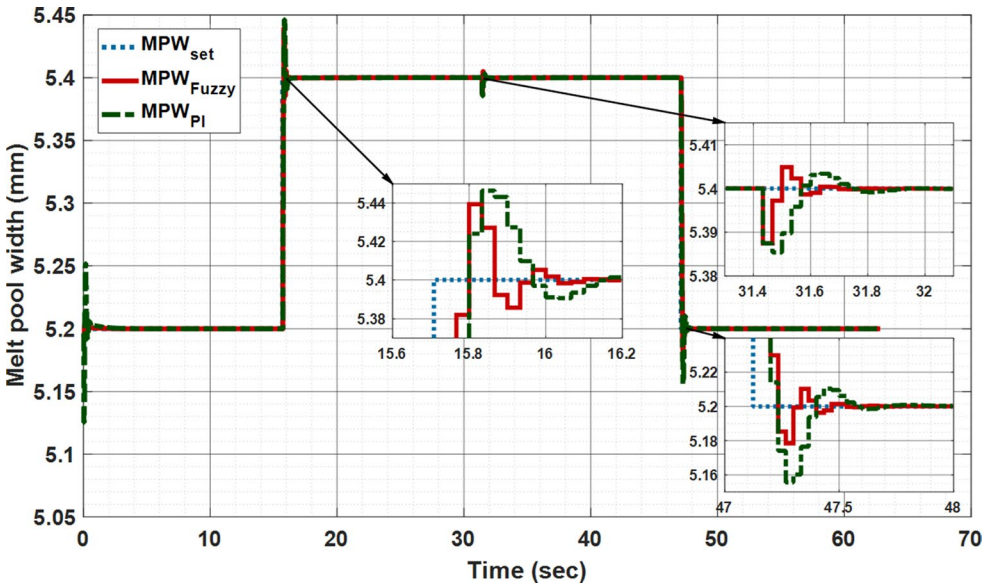

Fig. 11 Comparison of FLC and PI Controllers in Controlling MPW in the SISO L-DED/W Process

3.3.2 MIMO closed-loop control of MPW and hardness using PSQ and FLC

Following the definition of the FLC structure and the closed-loop control block diagram for the MIMO L-DED/W process developed with the PSQ framework, which is explained in the methodology section, the rule set of the FLC should be defined and hence applied to control MPW and hardness.

To establish the rule set, we must first understand the input-output relationships observed within the system. Considering the selected features for the F_2 model and observations of the first part of this study [8], the following general rules emerge:

- LP and MPW share a positive relationship.
- TS and MPW share a negative relationship.
- TS and R_{HC} share a positive relationship.
- LP and MPW have no direct effect on R_{HC}.

Based on these principles, the rule set for MPW and hardness control is detailed in Table 5, formatted as a matrix. This matrix outlines 18 configurations of input parameters. Given that LP and R_{HC} show no direct correlation and LP is excluded in the F_2 model, ΔLP should remain unaffected by the R_{HC} values. Instead, E_{MPW} and ΔE_{MPW} primarily influence ΔLP, aligning this with the SISO problem framework. Consequently, the ΔLP values for the first and second sets of nine rules mirror those defined for the SISO system. Determining ΔTS introduces additional complexity, as it impacts both R_{HC} and MPW. The adjustment of ΔTS is primarily influenced by $R_{HC,}$ emphasizing the prioritization of hardness maximization over control efficiency. For instance:

- If R_{HC} is one, indicating a low probability of high-class hardness, then TS should increase irrespective of its effect on MPW, setting ΔTS to five for the initial nine rules.
- If R_{HC} is two, suggesting high hardness is likely, maintaining maximum TS could negatively impact MPW control, especially when E_{MPW} is positive (seen in Rules 12, 15, and 18). In these cases, reducing TS enhances the ability to manage MPW effectively without sacrificing hardness maximization. Since ΔTS values are unknown for Rules 12, 15, and 18, their values are respectively set as variables (r_1, r_2, r_3) to be optimized.

It is noteworthy that for the remaining rules in the second set, ΔTS values are configured to maximize TS while ensuring MPW is effectively controlled.

The FLC structure is now prepared for use in simulations, pending the identification of defined optimization parameters, including r_1, r_2, and r_3, ($r_i \in [1\ 5]$, $i = 1 \ldots 3$) in addition to previously defined parameters (r_E, $r_{\Delta E,}K_{TS}$, K_{LP}). Thus, a total of seven parameters require optimization. The rule parameters are integers from one to four, and the ranges for the remaining four parameters are as follows:

$$0.05 \leq r_E,\ r_{\Delta E} \leq 0.5, \quad 1 \leq K_{TS},\ K_{LP} \leq 100$$

These ranges are established through trial and error in preliminary simulations. During optimization, GA generates a set of parameters for each function call, conducts a 10-second simulation, during which the sum of absolute E_{MPW} values is calculated and minimized. The optimal solution found is:

Table 5 The rule set applied to the MIMO FLC

Rule number	FLC Inputs			FLC outputs		Rule Weight
	E_{MPW}	ΔE_{MPW}	R_{HC}	ΔLP	ΔTS	
Rule 1	1	1	1	1	5	1
Rule 2	2	1	1	2	5	1
Rule 3	3	1	1	3	5	1
Rule 4	1	2	1	2	5	1
Rule 5	2	2	1	3	5	1
Rule 6	3	2	1	4	5	1
Rule 7	1	3	1	3	5	1
Rule 8	2	3	1	4	5	1
Rule 9	3	3	1	5	5	1
Rule 10	1	1	2	1	5	1
Rule 11	2	1	2	2	4	1
Rule 12	3	1	2	3	$\mathbf{r_1}$	1
Rule 13	1	2	2	2	4	1
Rule 14	2	2	2	3	4	1
Rule 15	3	2	2	4	$\mathbf{r_2}$	1
Rule 16	1	3	2	3	4	1
Rule 17	2	3	2	4	4	1
Rule 18	3	3	2	5	$\mathbf{r_3}$	1

$$(r_E^*,\ r_{\Delta E}^*,\ K_{TS}^*,\ K_{LP}^*,\ r_1^*,\ r_2^*,\ r_3^*) = (0.231,\ 0.198,\ 51.2,\ 74.3,\ 2,\ 2,\ 2) \quad (5)$$

Applying Eq. 5 to the FLC and conducting a 10-second simulation, the outcomes are depicted in Fig. 12. The initial plot illustrates a comparison of the controller's performance before and after optimization. Manually selecting optimization parameters through trial and error would yield parameters of (0.6, 0.6, 20, 75, 4, 4, 4), which leads to non-optimized control of the MPW. Conversely, the optimized results demonstrate substantial improvement, as shown in the inset plots; the optimized MPW (represented by the solid red line) quickly reaches the setpoint without any overshoot. The sums of absolute errors for the optimized and non-optimized controllers are 0.07873 mm and 0.1073 mm, respectively, highlighting the enhanced effectiveness of the optimized FLC.

Additionally, the manipulated variables during the simulation are analyzed in the second plot. At 2.5 s, the controller's set point increases, causing a sudden rise in LP to boost MPW, though LP quickly saturates at its maximum. Despite this, since E_{MPW} remains positive, TS decreases (from 13 to 10.5 mm/s) to further assist in increasing MPW. This demonstrates the effectiveness of optimizing rule parameters (r_1, r_2, r_3). Setting all parameters to value 4 results in a SISO-like system between LP and MPW with TS consistently at its maximum, which does not leverage the MIMO system's capabilities. Conversely, setting them to 2, as in the optimized results, significantly enhances the MPW control during critical moments such as at 2.5 and 7.5 s. It's important to note that control over R_{HC} is maintained throughout, even when TS is reduced at 2.5 s to boost MPW, R_{HC} does not drop below zero, ensuring the likelihood of achieving high hardness remains high throughout the simulation.

Another noteworthy observation is that LP does not stay constant to maintain a constant MPW during deposition. A comparison of the average LP values between the 2.5–5 s interval and the 7.5–10 s interval, under identical conditions, shows a decrease of LP from 4106 W to 4084 W. This reduction is attributed to heat accumulation in the part, which reduces the amount of energy needed to maintain a fixed MPW over time. This phenomenon is also evident from the slight decreasing trend in LP observed between 2.5 and 5 s, despite all conditions and parameters remaining unchanged. These observations demonstrate that the L-DED/W simulator accurately captures the physical behavior of the process, i.e., as time progresses and heat builds up in the part, less energy is needed to maintain a stable melt pool.

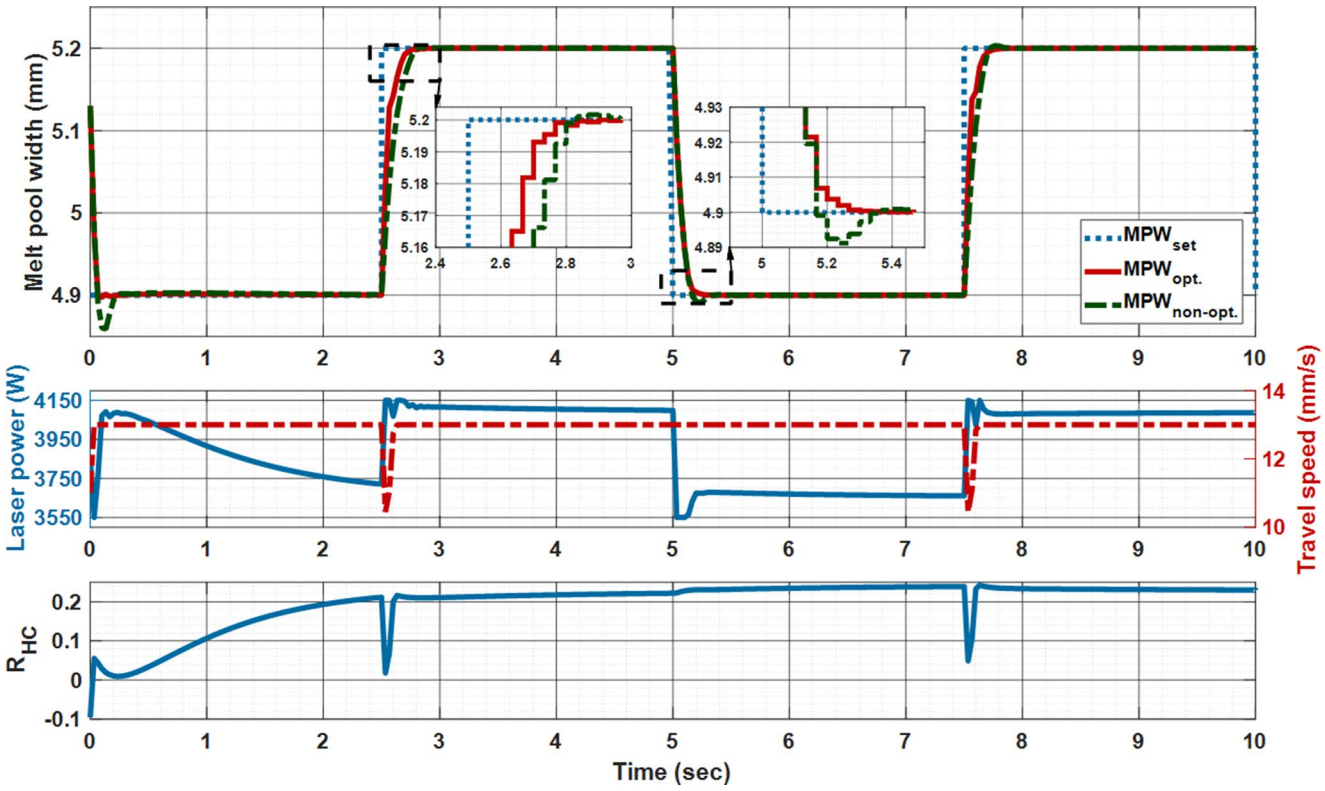

Fig. 12 MIMO control of MPW and hardness in the L-DED/W process. Comparison of optimized and non-optimized FLC controllers (top). LP, TS, and R_{HC} during simulation with optimized FLC controller (bottom)

3.3.3 MIMO Control Performance Under Input Perturbations

After fine-tuning the FLC, white Gaussian noises are added to the inputs ($\sigma_{TS} = 0.3726 \frac{mm}{s}$, $\sigma_{LP} = 114.96\,W$) to more closely mimic real-world variability. The effectiveness of our approach is demonstrated in Fig. 13, which displays the controlled MPW and its pre-set value, MPW_{set}, during a 10-second simulation with the uncertainty applied to the simulator model. The figure also shows the perturbed inputs (TS and LP), while the third-row plot illustrates that R_{HC} remains above zero throughout the simulation. Despite some fluctuations, the controller effectively maintains control over MPW, showcasing the controller's adaptability and robust performance even with input perturbations.

Overall, the application of MIMO and SISO closed-loop control strategies using the PSQ framework and FLC within the L-DED/W process leads to the following novel achievements and key findings:

- **First demonstration of in situ hardness-oriented closed-loop control in L-DED/W**: This study demonstrates, for the first time, the successful closed-loop control of hardness in a laser-directed energy deposition process. By leveraging the PSQ framework, hardness—an otherwise unmeasurable final quality during deposition—can be indirectly monitored and regulated in real time through melt pool signatures and process parameters.
- **Validation of FLC for MIMO regulation of geometric and mechanical properties**: FLC is shown to be an effective and robust control strategy for both MIMO and SISO systems in the L-DED/W process, enabling simultaneous regulation of deposition width and hardness-related outcomes. Unlike traditional model-based controllers such as PID or MPC, FLC does not require an explicit process model and effectively handles the nonlinearities and uncertainties inherent in additive manufacturing processes.
- **Demonstration of the essential role of the complete PSQ framework for quality control**:
- The results confirm that the integration of the full PSQ framework, particularly the F2 link between process signatures and final quality, is critical for successful quality-oriented control. Without this link, control performance degrades significantly, leading to steady-state errors and reduced accuracy, as also evidenced by prior comparative studies [7].

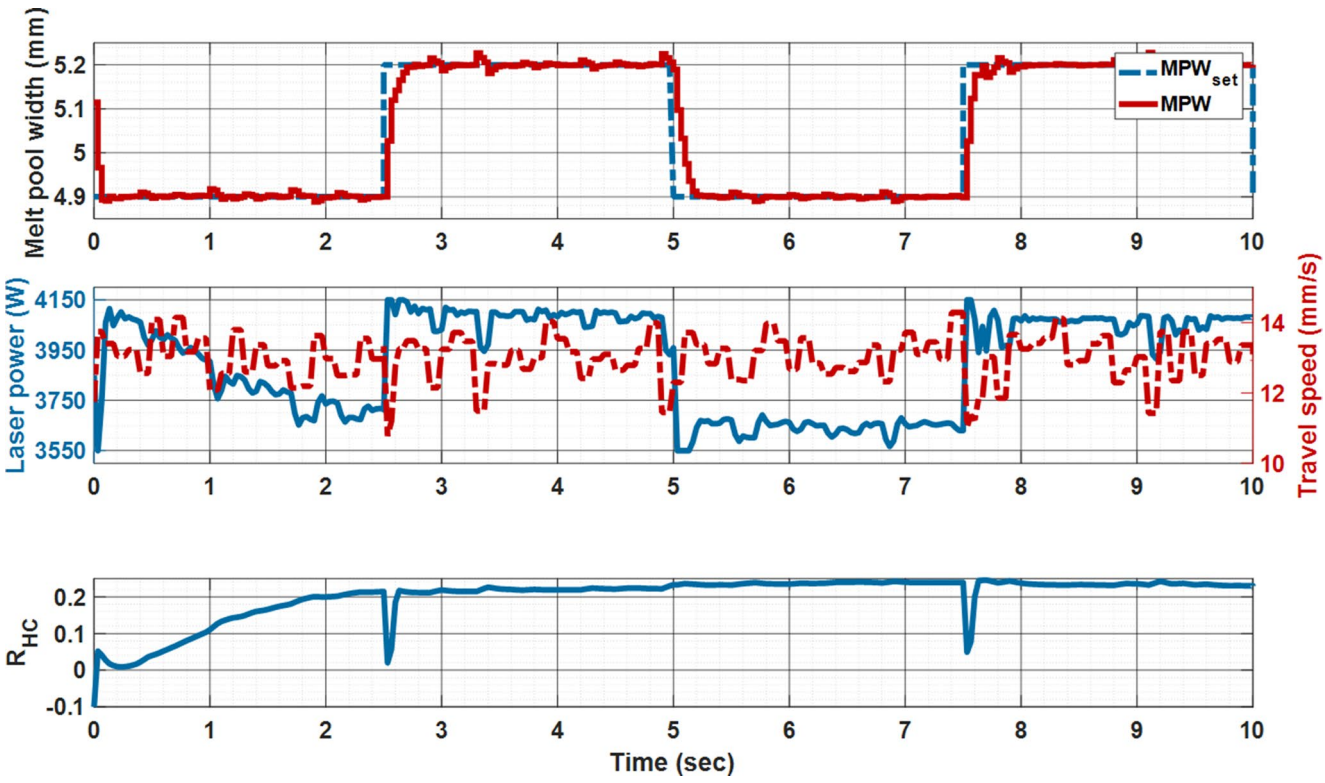

Fig. 13 Performance of the FLC for MPW and hardness control under uncertainty conditions

4 Conclusions

This study, as Part 2 of the series, advances in situ monitoring and closed-loop control for L-DED/W processes by demonstrating the application of the PSQ framework for MIMO control of otherwise in situ unmeasurable final qualities. Multi-objective control of hardness and geometric accuracy is achieved through three key stages. First, a MIMO LSTM model is developed for system identification, capturing the nonlinear relationships between process parameters (power and speed) and melt pool signatures, outperforming conventional models in predictive accuracy. Second, hardness is accurately classified using process parameters and melt pool signatures, enabling real-time indirect monitoring and control of final mechanical properties. Third, an FLC is integrated with the PSQ models to achieve simultaneous control of geometry and hardness, surpassing conventional PI controllers and representing the first successful application of FLC within the PSQ methodology for closed-loop MIMO control in DED processes.

Collectively, this work contributes by: (1) demonstrating high-fidelity MIMO system identification using LSTM networks; (2) showcasing the PSQ framework for in situ control of unmeasurable qualities such as hardness; and (3) establishing fuzzy logic control as an effective, computationally efficient strategy for multi-objective control in additive manufacturing. Future work will implement the models in real-world systems and generalize the framework using continuous, geometry-aware features—such as characteristic distances—to better capture heat accumulation, surrounding material effects, and scan strategy influences, enabling more robust, adaptive control across diverse deposition scenarios and geometries.

Acknowledgements The authors would like to express their sincere gratitude to Petter Hagqvist from Procada AB, whose expertise and assistance were instrumental in the successful execution of the experiments. The authors gratefully acknowledge funding from the Natural Sciences and Engineering Research Council (NSERC) of Canada [Grant numbers: RGPIN-2019-06601] and the affiliation with Eureka! SMART project (S0410) titled "TANDEM: Tools for Adaptive and Intelligent Control of Discrete Manufacturing Processes."

Author contributions • Mostafa Rahmani Dehaghani: Conceptualization, Methodology, Investigation, Programming, Writing-Original Draft, Validation, and Writing-Review and Editing.
• Farzaneh Farhang Mehr and Morgan Nilsen: Methodology, Visualization, and Writing-Review and Editing.
• Yifan Tang, Nguyen Gia Hien Vu, and Ke Wang: Data Curation, Visualization, and Writing-Review and Editing.
• Kevin Oldknow and G. Gary Wang: Conceptualization, Supervision, Project Administration, Funding Acquisition, and Writing-Review and Editing
The first draft of the manuscript was written by Mostafa Rahmani Dehaghani and all authors commented on previous versions of the manuscript. All authors read and approved the final manuscript.

Data availability The datasets generated and/or analyzed during the current study are available from the corresponding author upon reasonable request.

Declarations

Competing interests The authors declare that they have no competing interests.

Generative AI and AI-assisted technologies in the writing process During the preparation of this work, the authors used GPT-4o, developed by OpenAI, in order to improve the readability and language of the article. After using this tool, the authors reviewed and edited the content as needed and take full responsibility for the content of the publication.

References

1. Moges T, Ameta G, Witherell P (2019) A review of model inaccuracy and parameter uncertainty in laser powder bed fusion models and simulations. J Manuf Sci Eng. https://doi.org/10.1115/1.4042789
2. Olleak A, Xi Z (2020) Calibration and validation framework for selective laser melting process based on multi-fidelity models and limited experiment data. J Mech Des. https://doi.org/10.1115/1.4045744
3. Rahmani Dehaghani M, Tang Y, Gary Wang G (2022) Iterative uncertainty calibration for modeling metal additive manufacturing processes using statistical moment-based metric. J Mech Des. https://doi.org/10.1115/1.4055149
4. King WE, Barth HD, Castillo VM et al (2014) Observation of keyhole-mode laser melting in laser powder-bed fusion additive manufacturing. J Mater Process Technol 214:2915–2925. https://doi.org/10.1016/j.jmatprotec.2014.06.005
5. Ahn D-G (2021) Directed energy deposition (DED) process: state of the art. Int J Precis Eng Manuf-Green Technol 8:703–742. https://doi.org/10.1007/s40684-020-00302-7
6. Cai Y, Xiong J, Chen H, Zhang G (2023) A review of in-situ monitoring and process control system in metal-based laser additive manufacturing. J Manuf Syst 70:309–326. https://doi.org/10.1016/j.jmsy.2023.07.018
7. Rahmani Dehaghani M, Sahraeidolatkhaneh A, Nilsen M et al (2024) System identification and closed-loop control of laser hot-wire directed energy deposition using the parameter-signature-quality modeling scheme. J Manuf Process 112:1–13. https://doi.org/10.1016/j.jmapro.2024.01.029
8. Rahmani Dehaghani M, Oldknow K, Nilsen M et al (2025) In-Situ monitoring and control of Laser-Directed energy deposition with Wire – Part 1: Parameter-Signature-Quality analysis of duplex stainless steel. Submitted Journal of Manufacturing Processes
9. Hofman JT, Pathiraj B, van Dijk J et al (2012) A camera based feedback control strategy for the laser cladding process. J Mater Process Technol 212:2455–2462. https://doi.org/10.1016/j.jmatprotec.2012.06.027
10. Liang Z, Liao Z, Zhang H et al (2023) Improving process stability of electron beam directed energy deposition by closed-loop control of molten pool. Addit Manuf 72:103638. https://doi.org/10.1016/j.addma.2023.103638
11. Mantell SP, Wachtor AJ, Flynn GS et al (2022) Automated melt pool characterization for defect detection in additive manufacturing. In: Zelinski ME (ed) Appl Mach Learn 2022. SPIE, pp 24–30
12. Rahmani Dehaghani M, Pouyan S, Yifan T et al (2025) MIMO system identification and uncertainty calibration with a limited

amount of data using transfer learning. Int J Syst Sci 56:598–617. https://doi.org/10.1080/00207721.2024.2408526
13. Kumar LJ, Nair GGK (2017) Laser metal deposition repair applications for Ti-6Al-4V Alloy. Mech, Mater Sci & Eng J 7
14. Sciammarella FM, Salehi Najafabadi B (2018) Processing parameter DOE for 316L using directed energy deposition. J Manuf Mater Process 2:61
15. Nassar AR, Keist JS, Reutzel EW, Spurgeon TJ (2015) Intra-layer closed-loop control of build plan during directed energy additive manufacturing of Ti–6Al–4V. Addit Manuf 6:39–52. https://doi.org/10.1016/j.addma.2015.03.005
16. Farshidianfar MH, Khajepour A, Gerlich A (2016) Real-time control of microstructure in laser additive manufacturing. Int J Adv Manuf Technol 82:1173–1186. https://doi.org/10.1007/s00170-015-7423-5
17. Farshidianfar MH, Khodabakhshi F, Khajepour A, Gerlich AP (2021) Closed-loop control of microstructure and mechanical properties in additive manufacturing by directed energy deposition. Mater Sci Eng A 803:140483. https://doi.org/10.1016/j.msea.2020.140483
18. Zadeh LA (1965) Fuzzy sets. Infect Control Hosp Epidemiol. https://doi.org/10.1016/s0019-9958(65)90241-x
19. Peri VM, Simon D (2005) Fuzzy logic control for an autonomous robot. In: NAFIPS 2005–2005 Annual Meeting of the North American Fuzzy Information Processing Society. IEEE, pp 337–342
20. Azadegan A, Porobic L, Ghazinoory S et al (2011) Fuzzy logic in manufacturing: a review of literature and a specialized application. Int J Prod Econ 132:258–270
21. Al-Saadi T, Rossiter JA, Panoutsos G (2022) Fuzzy logic control in metal additive manufacturing: a literature review and case study. IFAC-PapersOnLine 55:37–42
22. Hua Y, Choi J (2005) Adaptive direct metal/material deposition process using a fuzzy logic-based controller. J Laser Appl 17:200–210
23. Farshidianfar MH, Khajepour A, Zeinali M, Gelrich A (2013) System identification and height control of laser cladding using adaptive neuro-fuzzy inference systems. In: Kaierle S (ed) Proceedings of the 32nd International Congress on Applications of Lasers & Electro-Optics. Laser Institute of America, pp 615–623
24. Li Y, Li X, Zhang G et al (2021) Interlayer closed-loop control of forming geometries for wire and arc additive manufacturing based on fuzzy-logic inference. J Manuf Process 63:35–47